Resolution Improvement in a High-Power Magnetic Resonance Imaging Gradient Power Amplifier

Keqiu Zeng, *Member, IEEE*, Jelena Popovic, *Member, IEEE*, Gert Rietveld, *Senior Member, IEEE*, Saijun Mao, *Senior Member, IEEE*, Hui Yu, *Member, IEEE*, Liguo Wang, *Member, IEEE*, Kun Liu, *Member, IEEE*, and Zhiding Zhou, *Member, IEEE*

***Abstract*—High-resolution gradient power amplifiers are required to generate high-fidelity gradient fields in magnetic resonance imaging (MRI) systems. Various aspects of gradient power amplifiers have been the subject of research in the past years, however, systematic analysis and design methods for its resolution improvement have not been sufficiently addressed. This article addresses this research gap with comprehensive analysis and design methods for resolution improvement. First, a method for systematic resolution characterization of the MRI gradient power amplifier with gradient coil is proposed. Second, noise modeling with respect to the critical aspects in the system resolution degradation is developed and discussed. Third, the resolution improvement methods of bandwidth optimization, pseudorandom code modulation, and utilizing silicon carbide (SiC) switching power devices are proposed and analyzed, achieving a resolution at the one part in 10^6 level. Finally, the resolution improvement methods are experimentally validated in a 1000 V/400 A SiC gradient power amplifier. The experimental results show a 3.6 times reduction in the peak spurious signals and resolution improvement at all current levels and pulse lengths, compared to a conventional insulated gate bipolar transistor GPA. These results prove the validity of the proposed methods for resolution improvement in a high-power MRI gradient power amplifier, enabling future high-power and high-resolution amplifier designs.**

***Index Terms*—Gradient power amplifier (GPA), high-resolution amplifier, low noise converter, magnetic resonance imaging (MRI), noise suppression, silicon carbide (SiC).**

Manuscript received September 24, 2021; revised February 12, 2022; accepted March 20, 2022. Date of publication March 25, 2022; date of current version May 23, 2022. This work was supported in part by Philips Healthcare (Suzhou) Company, Ltd., in part by the University of Twente, in part by Fudan University, and in part by Shanghai Pujiang Program under Grant 20PJ1401500. Recommended for publication by Associate Editor M. Saeedifard. *(Corresponding author: Saijun Mao.)*

Keqiu Zeng is with the Philips Healthcare (Suzhou) Company, Ltd., Suzhou 215021, China, and also with Faculty of Electrical Engineering, Mathematics and Computer Science, University of Twente, 7522 NB Enschede, The Netherlands (e-mail: keqiu_zeng@163.com).

Jelena Popovic is with the Faculty of Electrical Engineering, Mathematics and Computer Science, University of Twente, 7522 NB Enschede, The Netherlands (e-mail: j.popovic@utwente.nl).

Gert Rietveld is with the Faculty of Electrical Engineering, Mathematics and Computer Science, University of Twente, 7522 NB Enschede, The Netherlands, and also with VSL, 654 2600 Delft, The Netherlands (e-mail: g.rietveld@utwente.nl).

Saijun Mao is with the Academy for Engineering & Technology, Center for Shanghai Silicon Carbide Power Devices Engineering & Technology Research, Fudan University, Shanghai 200433, China (e-mail: maosaijun@126.com).

Hui Yu, Liguo Wang, Kun Liu, and Zhiding Zhou are with the Philips Healthcare (Suzhou) Company, Ltd., Suzhou 215021, China (e-mail: yuhui5095@163.com; wlg123572_2@sina.com; liu_kun76@sohu.com; zzd1992ah@163.com).

Color versions of one or more figures in this article are available at https://doi.org/10.1109/TPEL.2022.3162385.

Digital Object Identifier 10.1109/TPEL.2022.3162385

I. Introduction

ULTRAHIGH resolution in magnetic resonance imaging (MRI) gradient power amplifiers (GPAs) is an essential requirement to achieve high-quality images; at the same time, it is a big challenge to achieve. The particular challenge of these switched-mode GPAs is to generate precise output currents with ultralow noise in arbitrary waveforms with a typical frequency range of tens of kilohertz and output power at million-volt-ampere level. The loads are gradient coils with inductance values of several hundred μH to one mH. In MRI systems, the GPA consists of three high-power amplifiers, which respectively drive the *x*, *y*, and *z* orientation gradient coil [1].

In MRI systems, the imaging signals are radio frequency signals, which need to be acquired with high signal-to-noise-ratio (SNR) via radio frequency coils. Scanning of the image is achieved by varying the gradient field. Noise in the gradient field will affect the sampling time accuracy, and the noise in the gradient field will affect the time resolution steps taken in the data sampling, and therefore directly impact the imaging quality [1]. Therefore, high-resolution gradient field is required to ensure high imaging quality. A typical sampling trajectory in a two-dimensional (2-D) image is illustrated in Fig. 1, where each dot represents a sampling point. This trajectory is realized via the gradient pulses generated by the *x*-axis and *y*-axis GPAs, respectively. The first line in the trajectory is obtained by a positive *x*-axis gradient pulse allowing to sample the data with a step (ΔK_{x}), until the right maximum *x*-position is reached. Then, a positive *y*-axis gradient pulse is applied to move the sampling position one line up (ΔK_{y}). Subsequently, negative *x*-axis gradient pulses are applied with the same time duration as the positive *x*-axis gradient pulses in the first line, until the sampling position is back to the left minimum position in the second line. By repeating the same process and reversing the polarity of the *x*-axis gradient at the edge of each line, the scanning trajectory will cover the full 2-D area [1].

The horizontal spacing and vertical spacing in the trajectory are defined by the step size ΔK_{x} and ΔK_{y}, respectively [1]. These step sizes are determined by integration of the gradient

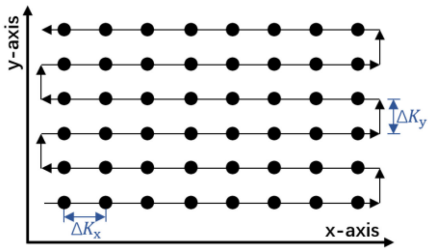

Fig. 1. Typical sampling trajectory for a 2-D MRI image [1].

strength generated by the GPA output current

$$\Delta \boldsymbol{K}_{\mathbf{x}} = \gamma \int_0^{\boldsymbol{\tau}_{\mathbf{ADC}}} \boldsymbol{G}_{\mathbf{x}} \boldsymbol{dt} \tag{1}$$

$$\Delta \boldsymbol{K}_{\mathbf{y}} = \gamma \int_0^{\boldsymbol{\tau}_{\mathbf{PE}}} \boldsymbol{G}_{\mathbf{y}} \boldsymbol{dt} \tag{2}$$

where G_x and G_y represents the x-axis gradient strength and y-axis gradient strength, respectively, τ_{ADC} denotes analog-to-digital converter (ADC) sampling period and τ_{PE} denotes the y-axis gradient pulse duration [1]. To achieve high resolution in the MRI imaging, a very high resolution of the GPA output current pulse is required, and the typical requirement is at the level of one part in 10^6.

In recent state-of-the-art literature, multiple converter topologies and soft-switching technologies have been studied to achieve the advantage of lower ripple current, lower electric stress, and increased flexibility at various power level GPAs [2]–[18]. It appears that the cascaded H-bridge is the most often used converter topology for the GPA application. Furthermore, several recent papers discuss the utilization of the newly emerging silicon carbide (SiC) switching power devices in GPAs [6]–[12]. High voltage SiC modules enable high switching frequency operation with lower power loss, enabling simpler architectures. Suppressing and reducing noise is critical to high-resolution applications such as for MRI, and therefore ripple cancellation filters have been studied and used to eliminate the switching frequency ripple in the output current [19]–[21]. Furthermore, noise and distortion minimization methods for a gallium nitride class-D amplifier used in nanoscale-precision positioning applications are presented in [22] and [23], which provide sufficient noise suppression and distortion reduction by using Kalman filters and delta–sigma modulation technology. In addition, an analysis for common mode noise is performed and the mechanism of the internal common mode resonance is analyzed for a GPA with cascaded H-bridges [24]. Moreover, dead-time compensation is another way to reduce the distortions of the amplifier [25]–[27]. Finally, low-jitter and low-noise gate drivers are studied and designed for reducing noise of the converter [28], [29], as well as research efforts to eliminate the jitter of digital isolators [30].

However, there is a lack of systematic and statistical investigation into the resolution characterization with respect to MRI GPA applications, which results in subpar resolution performance, more design iterations, and longer design cycle and validation time. In addition, the modeling and quantitative analysis of the critical factors influencing the GPA resolution has not been sufficiently addressed. Furthermore, flexible and efficient methods for improving GPA resolution are lacking. Since low noise hardware designs are complicated and expensive, high-performance filters will bring the challenges to the controller design, and advanced signal processing methods such as Kalman filter and delta–sigma modulation will introduce additional delays. Therefore, further research into more suitable methods for meeting the high-resolution requirements of GPAs is necessary, which is the focus of this article.

In this article, systematic analysis and design methods for the characterization and improvement of the resolution of MRI GPAs are presented. Furthermore, noise modeling and mathematical analysis methods with respect to the critical aspects causing degradation of the system resolution are developed and discussed in detail. Finally, approaches are proposed for the flexible and efficient resolution improvement, together with a demonstration of their validity in a high-power SiC GPA.

This article is organized as follows: Section II introduces a comprehensive method for resolution characterization in MRI GPA applications. Section III provides the modeling and mathematical analysis methods for the critical aspects causing GPA resolution degradation. Section IV proposes an effective solution for resolution improvement by minimizing various kinds of noise and disturbances in an MRI GPA. Section V validates the proposed methods with experimental results obtained in an SiC hardware demonstrator. Finally, Section VI summarizes the main findings of this article.

II. Resolution Characterization in MRI Gradient Power Amplifier

Noise and disturbance are the most common root-cause of the resolution degradation in MRI gradient systems. Therefore, it is critical to characterize and understand this impact mathematically. In this section, the statistical characteristics of noise is introduced first. Based on this, the resolution characterization in an MRI GPA system is presented in detail.

A. Statistical Characteristics of Noise

As the first step toward resolution analysis in MRI GPA, it is important to clarify the noise definition regarding power spectral density (PSD). For a continuous stationary random signal, the signal power can be calculated by measuring the energy of the signal within a time interval τ and dividing by τ. Thus, the average power P_{avg} of a signal $f(t)$ is equal to

$$\begin{aligned} \boldsymbol{P}_{\mathbf{avg}} &= \lim_{\boldsymbol{\tau}\to\infty} \frac{1}{\boldsymbol{\tau}} \int_0^{\boldsymbol{\tau}} \boldsymbol{f}^2(\boldsymbol{t}) \boldsymbol{dt} \\ &= \lim_{\boldsymbol{\tau}\to\infty} \frac{1}{\boldsymbol{\tau}} \int_{-\infty}^{+\infty} |\boldsymbol{F}_{\boldsymbol{\tau}}(\boldsymbol{f})|^2 \boldsymbol{df} = \int_{-\infty}^{+\infty} \boldsymbol{S}_{\boldsymbol{X}}(\boldsymbol{f}) \boldsymbol{df} \end{aligned} \tag{3}$$

where $F_\tau(f)$ is the Fourier transform of $f(t)$ signal in time interval of τ, and $S_X(f)$ is the normalized PSD [31], [32], which

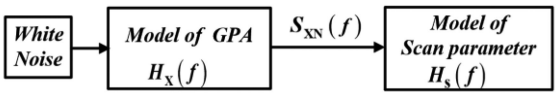

Fig. 2. Model of the MRI noise chain. $H_{\mathrm{X}}(f)$ indicates the model of the noise shaping by the GPAs. $H_{\mathrm{S}}(f)$ indicates the model of the MRI scan parameters.

can be expressed by the following:

$$S_{\mathbf{X}}(f) = \lim_{\tau\to\infty} \frac{|F_\tau(\mathrm{f})|^2}{\tau}. \tag{4}$$

The noise $s_n(t)$ generated by the noise chain has stochastic properties. The mean value of the noise signal $E[s_n(t)]$ therefore is expected to be zero, and the variance $D[s_n(t)]$ can be used to characterize the noise signal [31], [32]. Since the variance of the noise does not change over time, the mean value of the average power P_{avg} is the variance of the random process that generated $s_n(t)$, which can be obtained as follows:

$$\boldsymbol{D}[\boldsymbol{s_n}(\boldsymbol{t})] = \boldsymbol{E}\left[\boldsymbol{s_n^2}(\boldsymbol{t})\right] - (\boldsymbol{E}[\boldsymbol{s_n}(\boldsymbol{t})])^2 = \boldsymbol{E}(\boldsymbol{P_{avg}}). \tag{5}$$

The RMS value of the noise signal is equal to the square root of the average noise power. Therefore, the mean value of the RMS of the noise signal is equal to the standard deviation σ [31], [32]

$$\boldsymbol{\sigma} = \sqrt{\boldsymbol{E}(\boldsymbol{P_{avg}})} = \boldsymbol{E}[\boldsymbol{s_{RMS}}(\boldsymbol{t})] = \sqrt{\int_{-\infty}^{+\infty} \boldsymbol{S_X}(\boldsymbol{f})\,\boldsymbol{df}}. \tag{6}$$

This equation leads to the conclusion that an estimation of the variance of the noise signal in the time domain can equivalently be derived from its PSD. Having the PSD of a noise signal enables the derivation of stochastic characteristics of a signal derived from that noise by linear filtering, in particular the standard deviation or variance of the signal.

B. Resolution Characterization in MRI and Gradient Power Amplifiers

In an MRI system, variations of the spin phase at the field of view (FOV) are caused by random magnetic field variations [1]. Thus, the characteristic parameter of the imaging artifact is the standard deviation of the phase variation. This in turn is equal to a weighted integration over time of the variation, where the weighing function depends on the electronic devices used and the MRI scan parameters. The MRI noise chain, which characterizes these noise signals, is illustrated in Fig. 2. In this noise chain model, white noise is transferred to band-limited noise $S_{\mathrm{XN}}(f)$ by the model of the electronic subsystems such as the GPAs, followed by subsequent shaping by the model of the system scan parameters, which depends on the MRI pulse waveform. This output band-limited noise can be represented in the form of a standard deviation, and thus is directly linked to the resolution performance.

In MRI, the purpose of imaging is to determine the spin density $\rho(z)$ of a sample from an MRI signal $s_{\mathrm{MRI}}(t)$ [1], [37]. The 1-D MRI imaging equation [1] can be written as follows:

$$\boldsymbol{s_{MRI}}(\boldsymbol{t}) = \int \rho(\boldsymbol{z}) \boldsymbol{e}^{\mathbf{i}\phi_{\mathbf{G}}(\mathbf{z},\mathbf{t})} \boldsymbol{dz}. \tag{7}$$

The MRI image can be obtained by inverse Fourier transform of (7). The gradient magnetic field is the critical factor to determine the phase $\phi_{\mathrm{G}}(z,t)$ in (7), which can be expressed as follows:

$$\phi_{\mathbf{G}}(\boldsymbol{z},\boldsymbol{t}) = -\boldsymbol{z}2\pi\boldsymbol{\gamma}\int_0^{\mathbf{t}} \boldsymbol{G}(\boldsymbol{\tau})\boldsymbol{d\tau} \tag{8}$$

where γ denotes the gyromagnetic ratio [1], [37]. Equations (7) and (8) can be applied to gradient magnetic fields with any arbitrary orientation, and can be generalized by replacing $\phi_{\mathrm{G}}(z,t)$ by the phase due to all gradient field variations.

As a consequence, the GPA output noise current can be translated to the gradient magnetic field noise by multiplying with the gradient coil efficiency (*k*), which is defined as the ratio of gradient field generated to current drawn (with unit $\mu\mathrm{T/m/A}$ [38]–[40]), and the distance (*d*) to the center of an MRI system, which is half of the FOV. Therefore, (8) can be expressed as a function of the GPA output current I_{G} as follows:

$$\begin{aligned}\phi_{\mathbf{G}}(\boldsymbol{t}) &= -2\pi\boldsymbol{\gamma}\int_0^{\mathbf{t}} \boldsymbol{G}(\boldsymbol{\tau})\boldsymbol{d\tau} \\ &= -2\pi\boldsymbol{\gamma}\int_0^{\mathbf{t}} \boldsymbol{dkI_G}(\boldsymbol{t}-\boldsymbol{\tau})\boldsymbol{h_{int}}(\boldsymbol{\tau})\boldsymbol{d\tau}.\end{aligned} \tag{9}$$

It can be seen that the minimum resolution step size defined in (1) and (2) is presented in MRI 1-D imaging (7) with the phase (8) and (9). The resolution characteristic of the gradient magnetic field can be defined as the standard deviation of the phase $\phi_{\mathrm{G}}(t)$, and the gradient field is generated by the GPA output current. Therefore, the system resolution indicator can be defined as follows:

$$\begin{aligned}\sigma(\phi_{\mathbf{G}}(\boldsymbol{t})) &= 2\pi\boldsymbol{\gamma}\boldsymbol{kd}\sigma\left(\int_0^{\mathbf{t}} \boldsymbol{I_G}(\boldsymbol{t}-\boldsymbol{\tau})\boldsymbol{h_{int}}(\boldsymbol{\tau})\boldsymbol{d\tau}\right) \\ &= 2\pi\boldsymbol{\gamma}\boldsymbol{kd}\sigma\left(\int_0^{\mathbf{t}} \boldsymbol{s_{xn}}(\boldsymbol{t}-\boldsymbol{\tau})\boldsymbol{h_{int}}(\boldsymbol{\tau})\boldsymbol{d\tau}\right)\end{aligned} \tag{10}$$

where $h_{\mathrm{int}}(\tau)$ represents the noise gain of the system scan parameters which depends on the MRI pulse waveform, and $s_{\mathrm{xn}}(t)$ is the band-limited noise in the gradient output current. In conventional MRI systems, the FOV is about 45 cm and the gradient coil efficiency is about 45 $\mu\mathrm{T/m/A}$. Three degrees variation in phase is acceptable, which corresponds to a 15 μAs resolution requirement in GPA output current; this sets the limitation for the repeatability of gradient current pulses. To reach 15 μAs in a typical 400 A and 10 ms trapezoidal pulse, a resolution requirement of 1.5 mA in the amplitude of current pulse is required, which is at the level of 1 part in 10^6.

C. Resolution Modeling in Gradient Power Amplifier

As shown in Fig. 2, the output noise can be represented in time domain by the convolution with the system scan parameters

$h_{\text{int}}(t)$ as follows:

$$s_{\mathbf{out}}(t) = \int_0^{\infty} s_{\mathbf{xn}}(t-\tau) h_{\mathbf{int}}(\tau)\, d\tau. \tag{11}$$

Similarly, in the frequency domain, if a signal with spectrum density $S_{\text{in}}(f)$ is applied to a linear time-invariant system $H(f)$, then the output spectrum density $S_{\text{Xout}}(f)$ is given by the following [31], [32] :

$$S_{\mathbf{Xout}}(f) = S_{\mathbf{in}}(f)\,|H(f)|^2. \tag{12}$$

In GPAs, the gradient waveform is typically a trapezoidal waveform with short rising and falling edges, which can be approximated as a square waveform with the duration T_{echo}

$$h_{\mathbf{int}}(t) = \begin{cases} 1, 0 \le t \le T_{\mathbf{echo}} \\ 0, Otherwise \end{cases}. \tag{13}$$

Therefore, the system scan parameters $h_{\text{int}}(t)$ in the GPA can be written in Fourier transformation as follows:

$$H_{\mathbf{int}}(f) = G_{\mathbf{int}}(f) = T_{\mathbf{echo}} Sinc(\pi f T_{\mathbf{echo}})\, e^{-\mathrm{j}\pi f \mathbf{T_{echo}}}. \tag{14}$$

Combining (6), (12), and (14), the required system resolution in (10) can be derived as follows:

$$\begin{aligned} \sigma(\phi_{\mathbf{G}}(t)) &= 2\pi\gamma k d\sigma\left(\int_0^{\mathbf{T_{echo}}} I_{\mathbf{G}}(t-\tau)\, h_{\mathbf{int}}(\tau) d\tau\right) \\ &= 2\pi\gamma k d\sqrt{\int_{-\infty}^{+\infty} S_{\mathbf{XN}}(f)\,|G_{\mathbf{int}}(f)|^2 df} \end{aligned} \tag{15}$$

with $2\pi\gamma kd$ a constant in an MRI system. This model translates the MRI system resolution characteristic, which depends on the spin phase variation, to the resolution characteristic of GPA output current pulse expressed in the form of a standard deviation, which is equal to the GPA output current noise value. Therefore, the GPA resolution characteristic indicator can be defined as follows:

$$\sigma(I_{\mathbf{G}}) = \sigma\left(\int_0^{\mathbf{T_{echo}}} I_{\mathbf{G}}(t-\tau)\, h_{\mathbf{int}}(\tau) d\tau\right). \tag{16}$$

Smaller values of the resolution characteristic indicator $\sigma(I_{\text{G}})$ means less deviation in $\phi_{\text{G}}(t)$, and thus smaller deviation of the steps in the sampling shown in Fig. 1. Thus, GPA resolution improvement can be identified by reducing the value of $\sigma(I_{\text{G}})$. The MRI resolution and the GPA resolution can thus be improved by suppressing the noise in GPA output current.

III. Resolution Analysis Method for MRI Gradient Power Amplifier

A. System Modeling for Resolution Analysis

As shown in the previous section, GPA resolution can be improved by noise suppression. The noise sources, which have a critical impact on the GPA resolution performance, can be divided into two different types. The first type is quantization noise, which includes ADC quantization noise and pulsewidth modulation (PWM) quantization noise. The second type of noise is generated by the analog devices, primarily the jitter of the gate driver and the switching power devices, and the disturbance in the dc power supply. Fig. 3 illustrates a GPA system with these noise sources. The circuit model of the GPA load, which is a gradient coil, can be sufficiently accurately described as an inductor *L* and a series resistor *R* in the frequency range of interest [38]–[41].

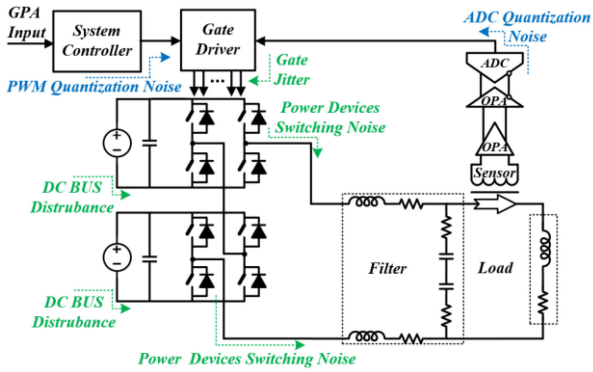

Fig. 3. GPA system with relevant noise sources: quantization noise sources (blue) and the disturbances of analog devices (green).

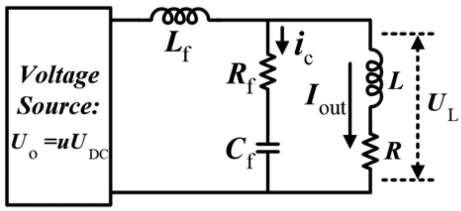

Fig. 4. Simplified circuit diagram of the GPA power stage. U_{DC} is the total dc voltage applied to the H-bridges. A zero-order hold approximation is used to represent the H-bridges output by uU_{DC}.

In order to analyze the impact in resolution from each type of noise source, a mathematical system model can be derived by the continuous-time state equations. By selecting the current i_{c} through the filter capacitor, the output current i_{out} and the output voltage u_{out}, the continuous-time state equations can be derived in the Laplace transformation form as follows:

$$sLI_{\mathbf{out}} + RI_{\mathbf{out}} = U_{\mathbf{L}} \tag{17}$$

$$sC_{\mathbf{f}}U_{\mathbf{L}} - sC_{\mathbf{f}}R_{\mathbf{f}}I_{\mathbf{c}} = I_{\mathbf{c}} \tag{18}$$

$$sL_{\mathbf{f}}I_{\mathbf{c}} + sL_{\mathbf{f}}I_{\mathbf{out}} = uU_{\mathbf{DC}} - U_{\mathbf{L}} \tag{19}$$

where u denotes the duty cycle generated by the controller; the other parameters can be found in the simplified GPA power stage model illustrated in Fig. 4.

Using these continuous-time state equations, the transfer functions of i_{out} to u, u_{out} to u, and i_c to u can be derived as follows:

$$G_{\mathbf{i_{out}/u}}(s) = \frac{I_{\mathbf{out}}}{u} = \frac{U_{\mathbf{DC}}(sC_{\mathbf{f}}R_{\mathbf{f}}+1)}{s^3L_{\mathbf{f}}C_{\mathbf{f}}L + s^2A + sB + R} \tag{20}$$

$$A = L_{\mathbf{f}}C_{\mathbf{f}}R + L_{\mathbf{f}}C_{\mathbf{f}}R_{\mathbf{f}} + LC_{\mathbf{f}}R_{\mathbf{f}} \tag{21}$$

$$B = L_{\mathbf{f}} + L + C_{\mathbf{f}}R_{\mathbf{f}}R \tag{22}$$

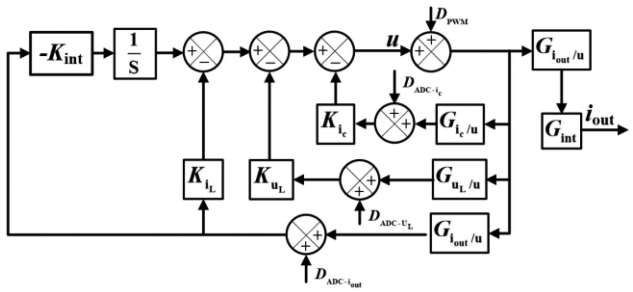

Fig. 5. Noise and disturbance model of the GPA system using the continuous-time state equations. This model includes the GPA converter, control system, gradient output filter and gradient coil. G_{int} represents the model of system scan parameters. $D_{\text{ADC}-\text{i}_{\text{out}}}$, $D_{\text{ADC}-\text{i}_{\text{c}}}$, $D_{\text{ADC}-\text{U}_{\text{L}}}$ and D_{PWM} denote the ADC and PWM quantization noise and disturbance.

$$\boldsymbol{G}_{\mathbf{u_L/u}}(\boldsymbol{s}) = \frac{\boldsymbol{U}_{\mathbf{L}}}{\boldsymbol{u}} = (\boldsymbol{sL}+\boldsymbol{R})\,\boldsymbol{G}_{\mathbf{i_{out}/u}}(\boldsymbol{s}) \tag{23}$$

$$\boldsymbol{G}_{\mathbf{i_c/u}}(\boldsymbol{s}) = \frac{\boldsymbol{I}_{\mathbf{c}}}{\boldsymbol{u}} = \frac{\boldsymbol{sC_f}(\boldsymbol{sL}+\boldsymbol{R})}{1+\boldsymbol{sC_fR_f}}\boldsymbol{G}_{\mathbf{i_{out}/u}}(\boldsymbol{s}). \tag{24}$$

These models can be used to simulate the hardware behavior. As a consequence, the mathematical model for the further noise chain analysis can be illustrated as in Fig. 5.

The model of system scan parameters G_{int} in Fig. 5 is an integration function, which can be approximated by (14) and can also be presented in Laplace transformation as follows:

$$\boldsymbol{G}_{\mathbf{int}} = \frac{1}{\boldsymbol{s}}\left(1-\boldsymbol{e}^{-\mathbf{sT_{int}}}\right). \tag{25}$$

Here T_{int} denotes the gradient pulse duration, which is in the level of milliseconds, meaning that the bandwidth of G_{int} is less than 1 kHz.

B. Resolution Analysis for the Impact of Quantization

ADC and full-digital PWM are the two key contributors of quantization noise in a GPA. The RMS value of the noise, which is equal to the standard deviation of the noise power, can be derived with the weight (q) of the minimum quantization step [36] as follows:

$$\sigma_{\mathbf{Quantization}} = \frac{\boldsymbol{q}}{\sqrt{12}}. \tag{26}$$

In the ADC, q is equal to the weight of one least significant bit and can also be represented by the SNR and full span (FS) of input signal. Thus, the ADC quantization noise becomes the following:

$$\sigma_{\mathbf{ADCNoise}} = \frac{\boldsymbol{FS}}{\sqrt{8}\,10^{\left(\frac{\mathbf{SNR}}{\mathbf{20}}\right)}}. \tag{27}$$

As a consequence, the one-side power spectral density of the ADC quantization noise can be derived as follows:

$$\boldsymbol{S}_{\mathbf{ADCX}}(\boldsymbol{f}) = \frac{\sigma^2_{\mathbf{ADCNoise}}}{\boldsymbol{f}_{\mathbf{ADC}}/2}. \tag{28}$$

In the full-digital PWM generator, the PWM is generated by comparing the digital reference signal with a digital triangular wave. The quantization noise can be considered as the deviation of the exact pulse width from the digitalized pulse width. The weight q is equal to the weight of a minimum step T_{min} in a PWM period T_{PWM}, that is, $T_{\text{min}}/T_{\text{PWM}}$. In the cascaded H-bridge topology, the voltage in each H-bridge is reduced by the number of H-bridges (m), which leads to a reduction of the noise. Therefore, the PWM quantization noise and its one-side power spectral density can be expressed as follows:

$$\boldsymbol{\sigma}_{\mathbf{PWM}} = \frac{\boldsymbol{T}_{\min}}{\sqrt{12}\,\boldsymbol{m}\,\boldsymbol{T}_{\mathbf{PWM}}} \tag{29}$$

$$\boldsymbol{S}_{\mathbf{dPWM}}(\boldsymbol{f}) = \frac{\sigma^2_{\mathbf{PWM}}}{\boldsymbol{f}_{\mathbf{PWM}}/2}. \tag{30}$$

The noise is calculated over the Nyquist bandwidth $f_{\text{ADC}}/2$ or $f_{\text{PWM}}/2$, which are above 10 kHz. In the GPA, the bandwidth of interest is much less. Therefore, a correct noise gain model must be in place. From Fig. 5, the noise gain models of the quantization noise chains can be derived as follows:

$$\begin{aligned}\boldsymbol{G}_{\mathbf{DADCiout}}(\boldsymbol{s}) &= \frac{\boldsymbol{i}_{\mathbf{out}}(\boldsymbol{s})}{\boldsymbol{D}_{\mathbf{ADC-i_{out}}}(\boldsymbol{s})} \\ &= -\boldsymbol{G}_{\mathbf{i_{out}/u}}\left(\boldsymbol{K}_{\mathbf{int}}\frac{1}{\boldsymbol{s}}+\boldsymbol{K}_{\mathbf{i_L}}\right)\Big/\boldsymbol{Den}(\boldsymbol{s})\end{aligned} \tag{31}$$

$$\boldsymbol{G}_{\mathbf{DADCUL}}(\boldsymbol{s}) = \frac{\boldsymbol{i}_{\mathbf{out}}(\boldsymbol{s})}{\boldsymbol{D}_{\mathbf{ADC-U_L}}(\boldsymbol{s})} = \frac{-\boldsymbol{G}_{\mathbf{i_{out}/u}}\boldsymbol{K}_{\mathbf{u_L}}}{\boldsymbol{Den}(\boldsymbol{s})} \tag{32}$$

$$\boldsymbol{G}_{\mathbf{DADCic}}(\boldsymbol{s}) = \frac{\boldsymbol{i}_{\mathbf{out}}(\boldsymbol{s})}{\boldsymbol{D}_{\mathbf{ADC-i_c}}(\boldsymbol{s})} = \frac{-\boldsymbol{G}_{\mathbf{i_{out}/u}}\boldsymbol{K}_{\mathbf{i_c}}}{\boldsymbol{Den}(\boldsymbol{s})} \tag{33}$$

$$\boldsymbol{G}_{\mathbf{D_{PWM}}}(\boldsymbol{s}) = \frac{\boldsymbol{i}_{\mathbf{out}}(\boldsymbol{s})}{\boldsymbol{D}_{\mathbf{PWM}}(\boldsymbol{s})} = \frac{\boldsymbol{G}_{\mathbf{i_{out}/u}}}{\boldsymbol{Den}(\boldsymbol{s})} \tag{34}$$

$$\begin{aligned}\boldsymbol{Den}(\boldsymbol{s}) &= 1+\left(\boldsymbol{K}_{\mathbf{int}}\frac{1}{\boldsymbol{S}}+\boldsymbol{K}_{\mathbf{i_L}}\right)\boldsymbol{G}_{\mathbf{i_{out}/u}} \\ &\quad +\boldsymbol{K}_{\mathbf{u_L}}\boldsymbol{G}_{\mathbf{u_L/u}}+\boldsymbol{K}_{\mathbf{i_c}}\boldsymbol{G}_{\mathbf{i_c/u}}.\end{aligned} \tag{35}$$

Consequently, by utilizing these models and (15), (16), the GPA resolution indicators impacted by one of the three ADCs and the PWM quantization noise can be expressed by $\sigma_{\text{ADC}-\text{X}}(I_{\text{G}})$ and $\sigma_{\text{PWM}}(I_{\text{G}})$, respectively, as follows:

$$\begin{aligned}&\boldsymbol{\sigma}_{\mathbf{ADC-X}}(\boldsymbol{I}_{\mathbf{G}}) \\ &= \sqrt{\int_0^{\frac{1}{2}\mathbf{f_{ADC}}} \boldsymbol{S}_{\mathbf{ADCX}}(\boldsymbol{f})\,|\boldsymbol{G}_{\mathbf{DADCX}}(\boldsymbol{f})\,\boldsymbol{G}_{\mathbf{int}}(\boldsymbol{f})|^2 \boldsymbol{df}} \\ &= \frac{\boldsymbol{FS}}{2\sqrt{\boldsymbol{f}_{\mathbf{ADC}}}10^{(\boldsymbol{SNR}/\mathbf{20})}} \\ &\quad \sqrt{\int_0^{\frac{1}{2}\mathbf{f_{ADC}}} |\boldsymbol{G}_{\mathbf{DADCX}}(\boldsymbol{f})\,\boldsymbol{G}_{\mathbf{int}}(\boldsymbol{f})|^2 \boldsymbol{df}}\end{aligned} \tag{36}$$

$$\begin{aligned}&\boldsymbol{\sigma}_{\mathbf{PWM}}(I_{\mathbf{G}}) \\ &= \sqrt{\int_0^{\frac{1}{2}\mathbf{f_{PWM}}} S_{\mathbf{dPWM}}(f)\,|G_{\mathbf{D_{PWM}}}(f)\,G_{\mathbf{int}}(f)|^2 \mathrm{d}f}\end{aligned}$$

$$= \frac{\sqrt{f_{\mathbf{PWM}}}T_{\mathbf{min}}}{\sqrt{6}m}\sqrt{\int_0^{\frac{1}{2}\mathbf{f_{PWM}}} |G_{\mathbf{D_{PWM}}}(f)\,G_{\mathbf{int}}(f)|^2 \mathrm{d}f} \tag{37}$$

where G_{DADCX} denotes one of three ADC noise gain models in (31)–(33) and $G_{\mathrm{D_{PWM}}}$ is the PWM noise gain model of (34).

In a full-digital PWM, T_{min} is the minimum PWM counter time step which is determined by the PWM counter clock frequency and the number of externed asynchronous PWM bits [33]–[35]. Thus, (37) can also be represented with the PWM effective number of bits (ENOB) as follows:

$$\boldsymbol{\sigma_{\mathbf{PWM}}}(\boldsymbol{I_{\mathbf{G}}}) = \frac{1}{\sqrt{6\boldsymbol{f_{\mathbf{PWM}}}}2^{\mathbf{ENOB}}} \sqrt{\int_0^{\frac{1}{2}\mathbf{f_{PWM}}} |\boldsymbol{G_{\mathbf{D_{PWM}}}}(\boldsymbol{f})\,\boldsymbol{G_{\mathbf{int}}}(\boldsymbol{f})|^2 \boldsymbol{df}} \tag{38}$$

$$\boldsymbol{ENOB} = \boldsymbol{log_2^{\mathbf{mT_{PWM}/T_{min}}}}. \tag{39}$$

C. Resolution Analysis for the Impact of Analog Device Disturbance

The jitter of the gate driver and switching power semiconductors together with disturbances of the DC power supply are the two major influencing factors to the resolution degradation in a GPA.

The jitter of the gate driver and switching power semiconductor is generated by deviation from the ideal timing in the switch-on or switch-off actions. The standard deviation can be assumed to be the maximum deviation $\Delta_{\mathrm{gatemax}}$. Furthermore, these switching actions are uncorrelated with time and with other power devices. Thus, the variation of turn-ON duration caused by these jitters can be given by $\sqrt{2}\Delta_{\mathrm{gatemax}}$, and the standard deviation of the duty cycle in m cascaded H-bridge converters can be derived as follows:

$$\boldsymbol{\sigma_{\mathbf{u}}} = \frac{\sqrt{2}\boldsymbol{\Delta_{\mathbf{gatemax}}}}{\sqrt{\mathbf{m}\mathbf{T_{PWM}}}}. \tag{40}$$

Since the jitter from gate drivers and switching power semiconductors can be directly observed in the GPA output current, the noise gain model is the same as for the ADC sampling output current, that is, $G_{\mathrm{DADCiout}}(f)$ in (31). Therefore, the resolution indicator for the impact of the jitter from gate drivers and switching power devices can be calculated by the following:

$$\boldsymbol{\sigma_{\mathbf{GD}}}(\boldsymbol{I_{\mathbf{G}}}) = \frac{\boldsymbol{\sigma_{\mathbf{u}}}}{\sqrt{\frac{\boldsymbol{f_{\mathbf{PWM}}}}{2}}} \sqrt{\int_0^{\frac{1}{2}\mathbf{f_{PWM}}} |\boldsymbol{G_{\mathbf{DADCiout}}}(\boldsymbol{f})\,\boldsymbol{G_{\mathbf{int}}}(\boldsymbol{f})|^2 \boldsymbol{df}}. \tag{41}$$

The dc power supply disturbance is another leading factor influencing the resolution. It can be observed in the GPA model that the output voltage of the inverter can be represented by a constant voltage uU_{DC} during PWM intervals. Therefore, disturbances of the dc power supply voltage have a significant impact on the GPA resolution performance.

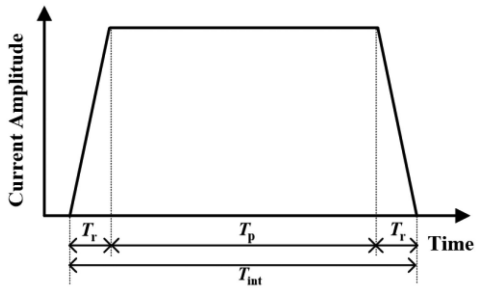

Fig. 6. Current waveform of a typical gradient pulse. T_{r} denotes the period of the rising-edge or the falling-edge. T_{p} denotes the plateau period.

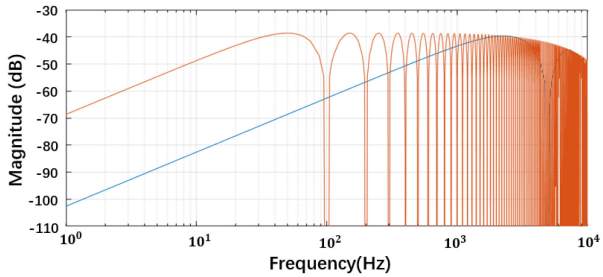

Fig. 7. Magnitude of $G_{\mathrm{DCbus}}(s) * G_{\mathrm{int}}$ for an integration time of 10 ms (orange) and 0.2 ms (blue). A state space model with integrator is used for the simulation.

In a typical gradient current waveform, as illustrated in Fig. 6, there are two different types of durations: the plateau period T_{p} and the period of rising-edge or falling-edge T_{r}. The controller and power supply in the gradient system have different behavior in these two time periods. During the rising-edge or falling-edge, the duty cycle generated by the controller is constant and at its maximum value, and the power supply generates the maximum deviation due to voltage droops or recharges. In the plateau period, the duty cycle has a small value and the power supply keeps a constant voltage with small ripple. In high-performance MRI systems, the period of the rising-edge or falling-edge is typically 0.2 ms.

The noise gain model of the dc power supply disturbance $G_{\mathrm{DCbus}}(s)$ is the same as the noise gain model of the digital PWM. However, the rising-edge period or falling-edge period T_{r} is different from the plateau time T_{p}. Therefore, the gains of G_{int} are different. Fig. 7 illustrates the two noise gain models of dc power supply disturbances with different pulse length.

In the GPA model, the output of the cascaded H-bridges can be presented by multiplying the duty cycle u , generated by the controller, with the actual dc power supply voltage $V_{\mathrm{dc.act}}$. However, if the nominal dc voltage $V_{\mathrm{dc.nom}}$ is used, then the effective duty cycle u_{eff} can be obtained by the following:

$$\boldsymbol{u_{\mathbf{eff}}}\boldsymbol{V_{\mathbf{dc.nom}}} = \boldsymbol{u}\boldsymbol{V_{\mathbf{dc.act}}}. \tag{42}$$

The effective duty cycle u_{eff} is the effective control value affecting the amplifier system. The disturbance on the overall dc voltage can be defined by its standard deviation $\sigma_{\mathrm{dc.act}}$, which is identical to its RMS value. Therefore, the noise on the effective control duty cycle u_{eff} caused by the dc voltage disturbance

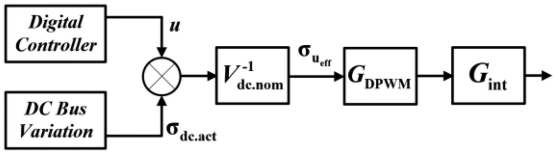

Fig. 8. Noise chain for variations in the dc power supply.

$\sigma_{\mathrm{dc.act}}$ is equal to the following:

$$\boldsymbol{\sigma_{u_{eff}}} = \frac{\boldsymbol{\sigma_{dc.act}} \boldsymbol{u}}{\boldsymbol{V_{dc.nom}}}. \tag{43}$$

The noise chain for variations in the dc power supply voltage is given in Fig. 8. The resulting maximum noise on the integral can be determined as follows:

$$\boldsymbol{\sigma_{DCbusM}} = \underbrace{\frac{\boldsymbol{u}}{\boldsymbol{V_{dc.nom}}} |\boldsymbol{G_{DCbus} G_{int}}|_{\boldsymbol{max}}}_{\boldsymbol{NG_{DC}}} \boldsymbol{\sigma_{dc.act}}. \tag{44}$$

In order to use (44) for the resolution estimation, the control duty cycle u needs to be calculated. Assuming a gradient coil with an effective resistance of 62 $\mathrm{m}\Omega$, an output voltage of 25 V will be required to maintain 400 A gradient output current during the plateau period, which requires a duty cycle *u* of 0.016 in the case of a 1500 V power supply voltage. The duty cycle *u* in the rising-edge or falling-edge period is nearly constant and equal to one. Beside this, the maximum magnitude of $G_{\mathrm{DCbus}}(s) * G_{\mathrm{int}}$ can be obtained in Fig. 7, which is -39.61 and -38.28 dB for the rising-edge or falling-edge period and the plateau period, respectively. By using these values, the gain NG_{DC} in (44) can be calculated, resulting in 6.97 and 0.13 $\mu\mathrm{As/V}$ for the rising-edge or falling-edge period and the plateau period, respectively. Therefore, the maximum noise on the integral of the two different periods can be determined as follows:

$$\boldsymbol{\sigma_{DCbusR}} = \boldsymbol{6.97 \sigma_{dc.act}} \tag{45}$$

$$\boldsymbol{\sigma_{DCbusP}} = \boldsymbol{0.13 \sigma_{dc.act}} \tag{46}$$

where σ_{DCbusR} denotes the standard deviation in the period of the rising-edge or falling-edge, and σ_{DCbusP} denotes the standard deviation in the plateau period. The value of σ_{DCbusR} is about fifty times higher than σ_{DCbusP}. Therefore, the GPA resolution indicator for the impact of the disturbance from the dc power supply can be evaluated by the following:

$$\boldsymbol{\sigma_{DC}}(\boldsymbol{I_G}) = \sqrt{\boldsymbol{2\sigma^2_{DCbusR} + \sigma^2_{DCbusP}}} \approx \sqrt{2} \boldsymbol{\sigma_{DCbusR}}. \tag{47}$$

It is obvious that the rising-edge and falling-edge are much more critical than the plateau period with respect to the GPA resolution. That means that variations in the length of the plateau period will not have a significant impact on the resolution.

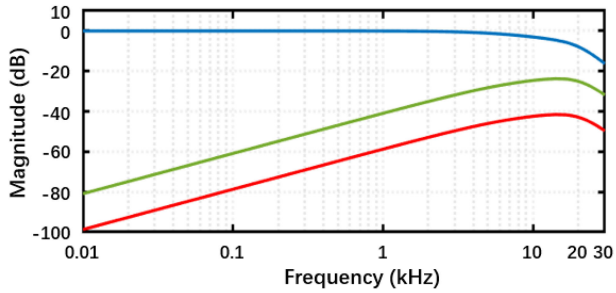

Fig. 9. Magnitude of the noise gain models: $G_{\mathrm{D_{ADCiout}}}(f)$ (blue), $G_{\mathrm{DADCic}}(f)$ (red), and $G_{\mathrm{D_{ADCUL}}}(f)$ (green). .

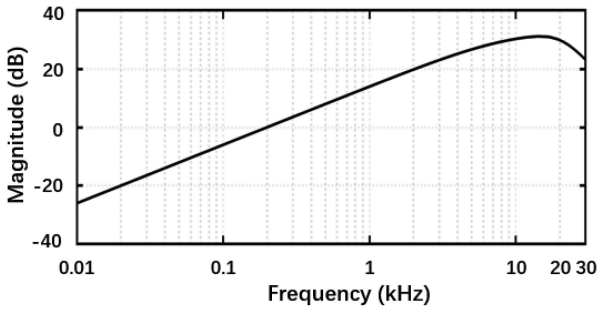

Fig. 10. Magnitude of the noise gain model $G_{\mathrm{D_{PWM}}}(f)$.

IV. Resolution Improvement Methods for MRI Gradient Power Amplifier

A. Bandwidth Optimization Method

In order to improve GPA and thus MRI resolution, both the quantization noise and the disturbances of the analog devices need to be suppressed. It can be observed in the resolution analysis equations that the noise gain models, defined in (31) to (35), play a critical role in resolution improvement. Moreover, the integration time T_{int} in the integration function $G_{\mathrm{int}}(f)$ is of the order of a millisecond in MRI applications. That means its corner frequency is below 1 kHz, which thus is the region of interest (ROI) for GPA resolution.

The magnitude of the noise gain models in 10 kHz bandwidth is illustrated as examples for further analysis in Figs. 9 and 10. The noise gains $G_{\mathrm{DADCUL}}(f)$, $G_{\mathrm{DADCic}}(f)$, and $G_{\mathrm{D_{PWM}}}(f)$ all have a bandpass characteristic with a linear ramp in the ROI. Therefore, system bandwidth optimization can efficiently attenuate the quantization noise. In order to minimize the impact of digital PWM quantization noise, the relationship of the GPA resolution indicator $\sigma_{\mathrm{PWM}}(I_{\mathrm{G}})$ defined in (37), system bandwidth and PWM ENOB needs to be studied, which are shown in Fig. 11. The impact of the PWM quantization effect can be ignored when the system bandwidth is higher than 5 kHz and ENOB is 14 bits which can be easily achieved in field programmable gate array (FPGA). The noise gain of $G_{\mathrm{D_{ADCiout}}}(f)$ has a low pass characteristic, so the bandwidth optimization approach is ineffective in suppressing the noise of the ADC sampling the output current. Thus, an ADC with higher SNR and suitable sampling frequency is required. Fig. 12 illustrates

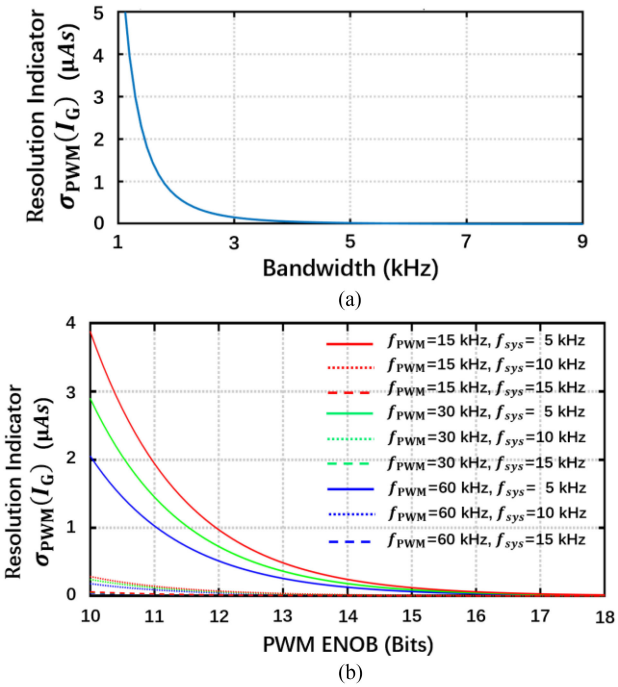

Fig. 11. (a) GPA resolution indicator $\sigma_{\mathrm{PWM}}(I_{\mathrm{G}})$ as a function of bandwidth at 30 kHz PWM switching frequency. (b) $\sigma_{\mathrm{PWM}}(I_{\mathrm{G}})$ as a function of ENOB for different values of the system bandwidth f_{sys} and PWM switching frequency f_{PWM}.

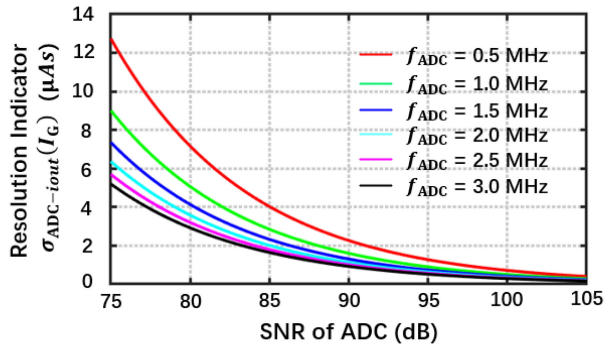

Fig. 12. GPA resolution indicator $\sigma_{\mathrm{ADC-iout}}(I_{\mathrm{G}})$ as a function of ADC SNR for different sampling rates f_{ADC}. The full ADC span is ±700 A and the pulse length is 10 ms.

the GPA resolution indicator $\sigma_{\mathrm{ADC-iout}}(I_{\mathrm{G}})$ defined in (36) as a function of ADC SNR. It is clear that the impact of the ADC quantization noise on the resolution can be ignored by selecting an ADC with SNR higher than 95 dB. Fig. 13 shows the GPA resolution indicator $\sigma_{\mathrm{ADC-UL}}(I_{\mathrm{G}})$ and $\sigma_{\mathrm{ADC-ic}}(I_{\mathrm{G}})$ defined in (36) as a function of bandwidth. Obviously, a 3 kHz bandwidth can effectively eliminate the quantization noise impact of these two ADCs. Thus, their impact can be ignored in the GPA resolution analysis.

The bandwidth optimization method can also effectively improve the GPA resolution under dc power supply disturbances. In the rising-edge or falling-edge, the dc voltage will be drooped or increased due to charging or discharging of the inductive load. A

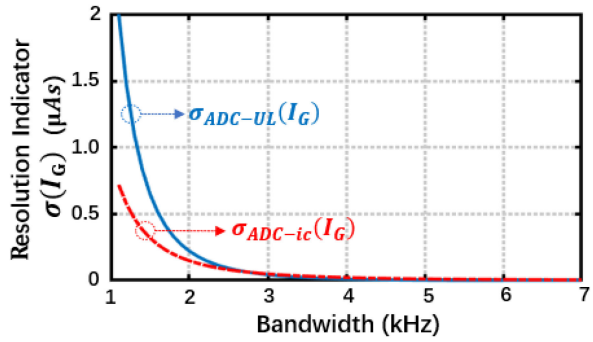

Fig. 13. GPA resolution indicator $\sigma_{\mathrm{ADC-UL}}(I_{\mathrm{G}})$ and $\sigma_{\mathrm{ADC-ic}}(I_{\mathrm{G}})$ as a function of bandwidth. SNR and sampling frequency of both ADCs are set to 80 dB and 1 MHz, respectively, in the simulation.

TABLE I
GPA RESOLUTION FOR DIFFERENT SYSTEM BANDWIDTHS UNDER DC POWER SUPPLY DISTURBANCE

System bandwidth	5 kHz	10 kHz	15 kHz
$\lvert G_{\mathrm{DCbus}}\rvert_{\max}$ (dB)	-38.6	-62.9	-76.8
σ_{DC} (μAs)	49.3	3.38	0.68

Note: $T_{\mathrm{r}} = 0.2$ ms, $T_{\mathrm{p}} = 10$ ms, $\sigma_{\mathrm{dc.act}} = 5$ V RMS and $V_{\mathrm{dc.nom}}$=1500 V.

TABLE II
SUMMARY OVERVIEW OF GPA RESOLUTION FOR DIFFERENT TYPE OF NOISE AND DISTURBANCE

	DC Power Supply Disturbance	*ADC Quantization Noise*	*Gate and Device Jitter*	*PWM Quantization Noise*
Resolution @ 10 kHz bandwidth (μAs)	3.38	1.00	0.5	< 0.1

Note: $f_{\mathrm{PWM}} = 30$ kHz , PWM ENOB $= 16$ bits , $f_{\mathrm{ADC}} = 1.0$ MSPS, ADC SNR = 95 dB, $\Delta_{\mathrm{gatemax}} = 20$ ns, $\sigma_{\mathrm{dc.act}} = 5$ V RMS, $V_{\mathrm{dc.nom}} = 1500$ V, pulse length is 10 ms.

variation of 5 V RMS in the overall dc voltage is normal, which is about 30 V peak-to-peak voltage droop. Consequently, σ_{DCbus} is equal to 49.3 μAs, which by far exceeds the 15 μAs resolution requirement. There are two methods to minimize this impact of dc power supply disturbance. The first method is dc voltage compensation [2]. The second method is to use the bandwidth optimization method. Table I illustrates the improvement of GPA resolution by increasing the system bandwidth. Obviously, higher system bandwidths can better suppress the impact of dc power supply disturbance. However, a high system bandwidth also leads to a high bandwidth in the low-pass noise gain $G_{\mathrm{D_{ADCiout}}}(f)$, which degrades the resolution by introducing more noise especially at low PWM switching frequency. Therefore, a 10 kHz system bandwidth is a good choice, which is already sufficient to achieve the 15 μAs aim. Table II summarizes the GPA resolution for different types of noise and disturbance and with the 10 kHz system bandwidth. It is evident that dc power supply disturbance is the major influencing factor.

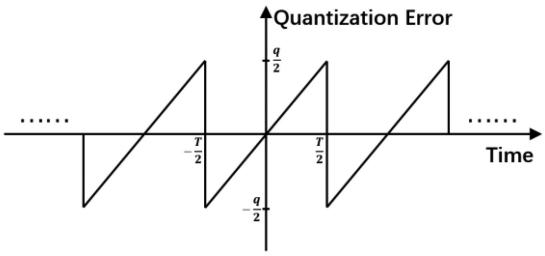

Fig. 14. Quantization error in a digital PWM generator.

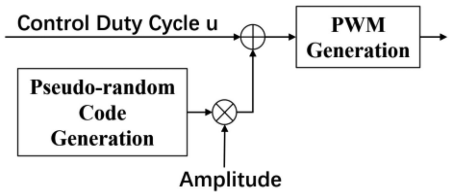

Fig. 15. Pseudorandom code modulation in a digital PWM generator.

B. Pseudorandom Code Modulation

By studying the MRI imaging (7)–(9), and (15), it is clear that the fixed-frequency spurious signals in the GPA output current will create disturbances in the MRI signal, in addition to the noise in the ROI. This effect will have a significant impact on the MRI resolution, in particular at the frequencies where the system scan parameter $h_{\text{int}}(t)$ has less filtering effectiveness. Therefore, next to reduction of noise, suppressing fixed-frequency spurious signals is necessary for resolution improvement.

In full-digital PWM generation, the impact of PWM noise can be further reduced with pseudorandom code modulation. In a digital PWM generator, the quantization error can be described as in Fig. 14 [36]. The Fourier transform can be written as follows:

$$\boldsymbol{F_{\mathrm{PWM}}}(\omega) = 2\pi \sum_{\mathbf{k}=-\infty}^{\mathbf{k}=+\infty} \boldsymbol{a_{\mathbf{k}}} \boldsymbol{\sigma}\left(\omega - \frac{2\boldsymbol{k}\pi}{\boldsymbol{T}}\right) \tag{48}$$

$$\boldsymbol{a_{\mathbf{k}}} = \pi\delta\left(\frac{2\boldsymbol{k}\pi}{\boldsymbol{T}}\right) - \frac{\boldsymbol{q}\,\boldsymbol{sin}\,(\boldsymbol{k}\pi)}{2\boldsymbol{k}\pi} - \boldsymbol{j}\frac{\boldsymbol{T}\,\boldsymbol{sin}\,(\boldsymbol{k}\pi)}{2(\boldsymbol{k}\pi)^2}. \tag{49}$$

It is obvious in (48) that the quantization process of the digital PWM will generate a noise spectrum with fixed frequencies, as the PWM quantization error has a periodic sawtooth waveform. By utilizing pseudorandom code modulation, the periodic sawtooth waveform will be distorted toward a random signal, and its noise spectrum will become similar to white-noise. Therefore, the impact of PWM quantization noise will be reduced. The block diagram of pseudorandom code modulation in a digital PWM generator is shown in Fig. 15.

C. Resolution Improvement by Utilizing SiC Switching Power Devices

SiC switching power devices have well-known benefits in lower power loss, higher switching frequencies and higher power densities [9]. In addition, SiC switching power devices can also improve GPA resolution.

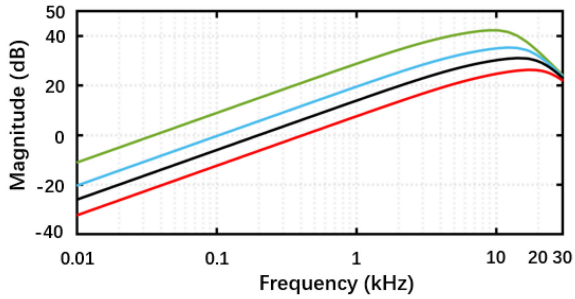

Fig. 16. Magnitude of noise gain model $G_{\mathrm{D_{PWM}}}(f)$ as a function of frequency for different system bandwidths. Bandwidth: 4 kHz (green), 8 kHz (blue), 10 kHz (black), 12 kHz (red).

The bandwidth optimization approach can gain higher noise attenuation value in the ROI. In this approach, the noise gain $G_{\mathrm{D_{PWM}}}(s)$ is critical to the noise suppression. When the high system bandwidth is used, the attenuation in the low frequency will be more significant.

GPAs can achieve higher bandwidths by utilizing SiC switching power devices, because SiC devices can reduce the dead time and operate at a high switching frequency. Fig. 16 depicts the magnitude of the noise gain $G_{\mathrm{D_{PWM}}}(s)$ for different system bandwidths in a SiC GPA. It can be clearly observed that the GPA with higher system bandwidth has better noise attenuation capability in the ROI. In addition, the noise gain model $G_{\mathrm{D_{PWM}}}(f)$ will amplify the spurious signals with the magnitude of the positive noise gain. The GPA with higher system bandwidth has the capability to move the frequency range with positive noise gain toward higher frequency, thereby reducing the impact on the system resolution. Moreover, the high switching frequency of the SiC switching power devices is much farther away from the required bandwidth compared with the GPA using insulated gate bipolar transistor (IGBT), which improves the effectiveness of the GPA output filter at the switching frequency and its harmonics. Therefore, the GPA resolution will be improved due to less fixed-frequency spurious signals. An experiment in Section V will prove this effectiveness.

V. Experimental Results

In order to validate the proposed analysis and design methods for resolution improvement, a GPA hardware demonstrator with 1000 V output voltage and 400 A output current has been built with SiC power modules as shown in Fig. 17, using the topology given in Fig. 3. The key components and experimental instruments are listed in Table III. A full-digital state space controller and PWM generator is built using an FPGA. This GPA is tested with an inductive load of 225 μH and 62 mΩ equivalent resistance. Fig. 18 shows the experimental waveform of a pulse sequence in the SiC GPA demonstrator with 400 A output current.

As mentioned above, a very high resolution in gradient output current pulse is required for an MRI system, typically at the

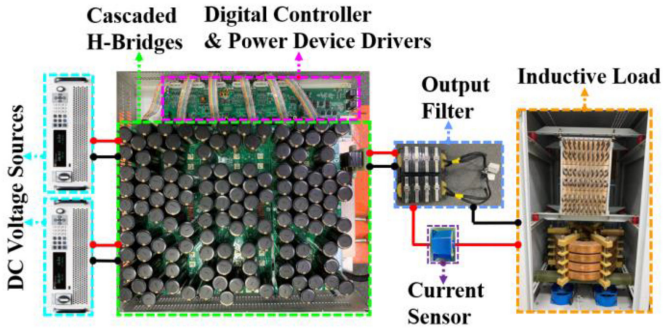

Fig. 17. Picture of key elements in the 1000 V/400 A GPA demonstrator.

TABLE III
KEY GPA COMPONENTS AND TEST EXPERIMENT INSTRUMENTS

Instrument	*Model Type*	*Parameter*
SiC Module	*CAB530M12BM3*	1200 V, 530 A
Current Sensor	*ITN 900-S*	900 A
Digital Control Board	*FPGA*	*Xilinx XC7Z100*
ADC	*LTC2378*	18 Bits, *SNR*: 100 dB
Operational Amplifier	*AD8676*	*Voltage noise:* 2.8 nV/√Hz @ 1 kHz
Output Filter	*LC Low Pass*	*L:* 60 µH, *C*: 220 nF
Output Load	*Inductive Load*	*L:* 225 µH, *R*: 62 mΩ
Current Probe	*CWT6*	1200 A, 16 MHz
DC Voltage Source	*IT6036B-800-150*	0 - 800 V, 0 - 150 A
Oscilloscope	*MDO4104B-3*	1 GHz

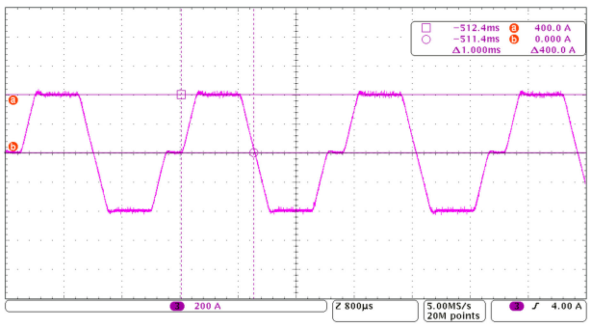

Fig. 18. Typical GPA experimental waveform with 400 A output current.

level of one part in 10^6. Therefore, a high-accurate measurement system is needed to detect and validate the GPA resolution improvements. A diagram of the digital measurement system is illustrated in Fig. 19, and its key components are listed in Table IV. The GPA output current is measured with a high-resolution zero-flux-based current sensor DS600ID with 0.02 ppm noise level below 1 kHz. The current signals are sampled at 1 MSPS by a 20-bit high-resolution ADC LTC-2378 with SNR of 104 dB. Then, the sampled data is digitally transferred by an FPGA controller to a computer for resolution calculation and comparison. The circuits and components in the measurement chain are placed in an electromagnetically shielded chamber to avoid any external interference during the experiments.

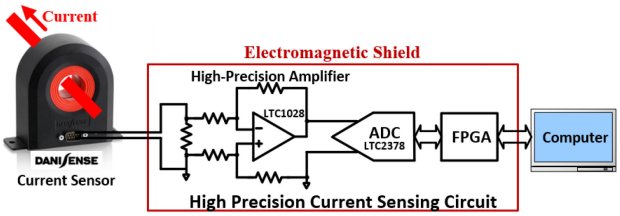

Fig. 19. Diagram of the high-accurate digital measurement system for verification of the GPA resolution improvements, based on a low-noise accurate current sensor.

TABLE IV
KEY COMPONENTS OF THE HIGH-ACCURATE MEASUREMENT SYSTEM

Instrument	*Model Type*	*Parameter*
Current Sensor	*DS600ID*	*Noise:* 0.02 *ppm below* 1 *kHz*
Operational Amplifier	*LTC1028*	*Noise*: 0.85 $nV/\sqrt{Hz}$ *at* 1 *kHz*
ADC	*LTC2378*	20 *Bits*
Digital Controller	*FPGA*	*Xilinx XC7Z100*

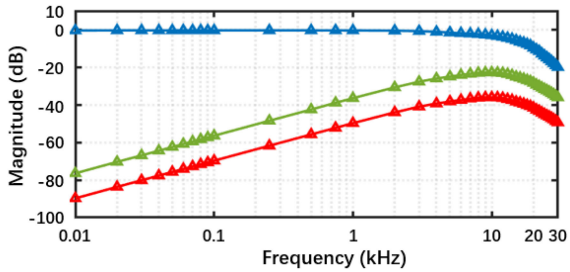

Fig. 20. Measured magnitude of ADC noise gain $G_{\mathrm{D_{ADCiout}}}(f)$ (blue), $G_{\mathrm{D_{ADCUL}}}(f)$ (red), and $G_{\mathrm{DADCic}}(f)$ (green) in the SiC GPA demonstrator with 10 kHz bandwidth.

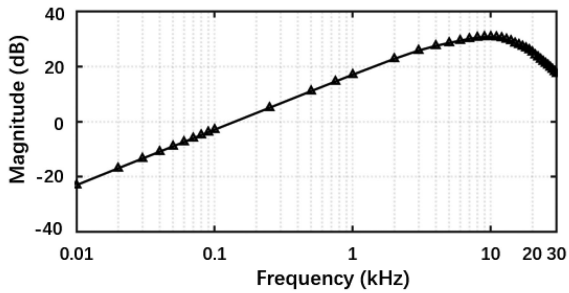

Fig. 21. Experimental results of the magnitude of the noise gain model $G_{\mathrm{D_{PWM}}}(f)$ as a function of frequency in the SiC GPA demonstrator with 10 kHz bandwidth.

The proposed methods for GPA resolution analysis and improvement are based on the noise gain models, mathematically presented by (31) to (35). Therefore, it is critical to validate the effectiveness of these built models in the GPA demonstrator. The magnitude of these noise gain models is tested in the GPA demonstrator as a function of frequency. The measurement results for a GPA implementation with 10 kHz system bandwidth are shown in Figs. 20 and 21, and can be validated by comparing these with the simulation results in Figs. 9 and 10. Obviously, the experimental results match well with the simulation results. The

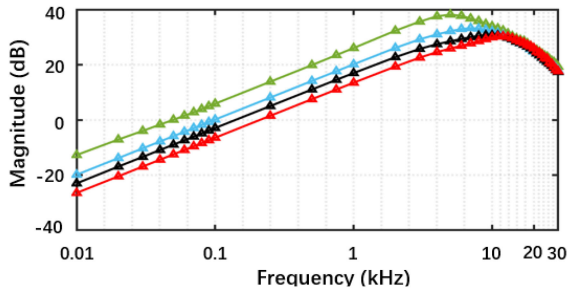

Fig. 22. Experimental results of the magnitude of noise gain $G_{\mathrm{D_{PWM}}}(f)$ as a function of frequency for different system bandwidths. Bandwidth: 4 kHz (green), 8 kHz (blue), 10 kHz (black), 12 kHz (red).

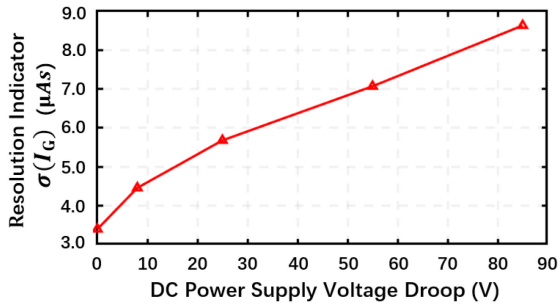

Fig. 23. GPA Resolution indicator $\sigma(I_{\mathrm{G}})$ as a function of dc power supply disturbance. The experiment is implemented with 6 kHz bandwidth.

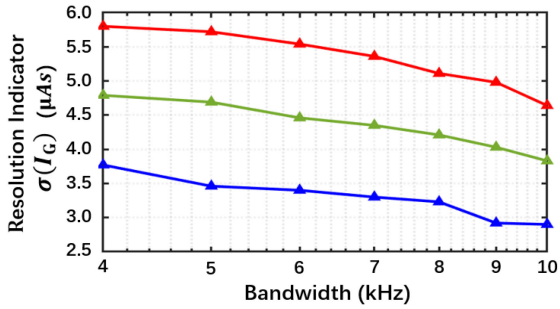

Fig. 24. GPA resolution indicator $\sigma(I_{\mathrm{G}})$ for different dc power supply disturbance levels ($V_{\mathrm{DC\_droop}}$) as a function of system bandwidth. Blue: $I_{\mathrm{out}} = 100$ A and $V_{\mathrm{DC\_droop}} = 0$ V ; Green: $I_{\mathrm{out}} = 200$ A and $V_{\mathrm{DC\_droop}} = 8$ V ; Red: $I_{\mathrm{out}} = 300$ A and $V_{\mathrm{DC\_droop}} = 25$ V . The pulse length is 25 ms.

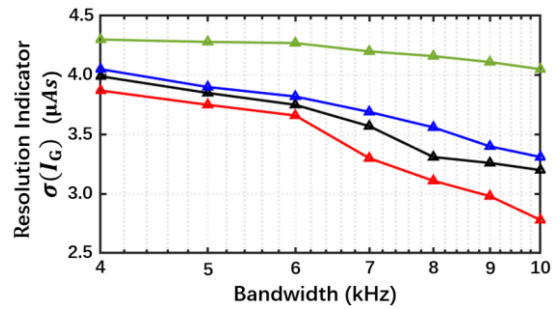

Fig. 25. GPA resolution indicator $\sigma(I_{\mathrm{G}})$ as a function of system bandwidth. Output current: 100 A (red), 200 A (black), 300 A (blue), 400 A (green). The dc bus voltage for each H-bridge is set to 650 V. The pulse length is 10 ms.

deviations in the frequency of the peak value and the noise attenuation value are caused by the inevitable differences between the actual hardware and the ideal components in the simulation. The noise gain model $G_{\mathrm{D_{PWM}}}(f)$ plays the most critical role in the noise suppression, so it is necessary to study its behavior as a function of different system bandwidths. Fig. 22 illustrates the experimental results on the SiC GPA for different system bandwidths. The experimental results show that $G_{\mathrm{D_{PWM}}}(f)$ has more than 10 dB noise attenuation in ROI at 10 kHz bandwidth, compared to a 4 kHz bandwidth. The agreement of these experimental results with the simulations shown in Fig. 16, validate the bandwidth optimization methods.

As analyzed in Section IV, dc power supply disturbances lead to significant reduction in GPA resolution, and the bandwidth optimization method can effectively reduce this impact. Fig. 23 shows the experimental results of the GPA resolution indicator $\sigma(I_{\mathrm{G}})$, defined in (16), as a function of different disturbance levels in the dc bus voltage. In this experiment, the rated current of the dc power supply is set to the low limit to create a voltage droop $V_{\mathrm{DC\_droop}}$ as the dc voltage disturbance, and the rated dc bus voltage for each H-bridge is 400 V. It can be seen that a dc voltage droop of 80 V increases $\sigma(I_{\mathrm{G}})$ by a factor of 3, leading to a very significant degradation in resolution. Fig. 24 shows the improvement in GPA resolution for different dc bus disturbance levels by the bandwidth optimization method. Obviously, higher bandwidth leads to less impact from dc power supply disturbances, and the resolution can be improved by more than 25 % by going to a 10 kHz system bandwidth. Fig. 25 shows additional tests of the GPA resolution indicator $\sigma(I_{\mathrm{G}})$ for different output currents and a shorter pulse length of 10 ms to reduce the impact of $V_{\mathrm{DC\_droop}}$. Compared with a 4 kHz bandwidth, it is evident that a 10 kHz bandwidth improves GPA resolution at all current levels. These experimental results prove the effectiveness of the proposed bandwidth optimization method for improving GPA resolution.

A key feature of the proposed resolution improvement methods next to the bandwidth optimization is the pseudorandom code PWM generation to provide additional suppression on disturbances at fixed frequencies. Experiments are performed with three different output currents, that is 50 A, 100 A, and 400 A, with results as shown in Fig. 26. From this figure, it is apparent that the pseudorandom code PWM generator indeed can effectively suppresses the spurious frequency components in the spectrum, leading to around 15%, 10%, and 13% peak reduction in peak spurious signal at 50, 100, and 400 A output currents, respectively. It validates the effectiveness of pseudorandom code PWM generation.

As analyzed in Section IV, SiC switching power devices have the ability to improve GPA resolution with respect to IGBT devices. To illustrate this, the noise performance of a SiC GPA demonstrator with two cascaded H-bridges is compared to that of a conventional IGBT GPA with three cascaded H-bridges. The resolution performance is compared by studying both the spectrum of the fixed-frequency spurious signals as well as the GPA resolution indicator $\sigma(I_{\mathrm{G}})$. The switching frequency in each power device is around 30 and 15 kHz for the SiC GPA

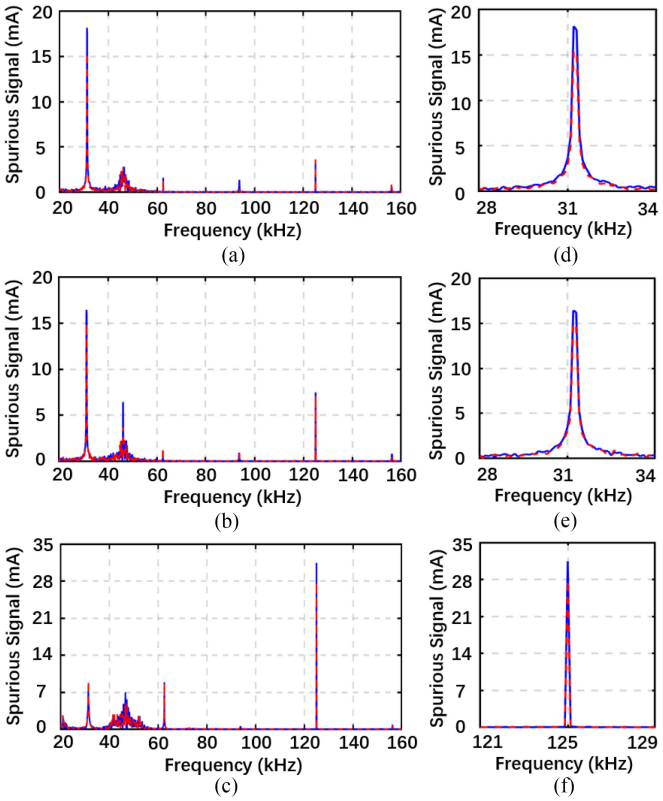

Fig. 26. Spectrum of the fixed-frequency spurious signals in GPA output current with (red dash) and without (blue solid) pseudorandom code modulation in PWM generation. (a), (b), (c) show the noise spectrum in 50, 100, 400 A output current, respectively. (d), (e), (f) show zooms of the peak spurious signal for 50, 100, 400 A output current, respectively.

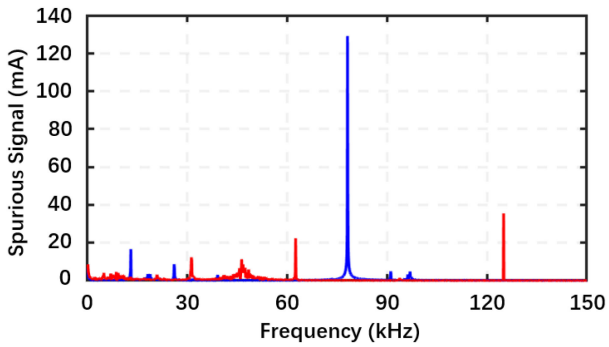

Fig. 27. Spectrum of fixed-frequency spurious signals at 400 A output current for the SiC GPA demonstrator (red) and a conventional IGBT GPA (blue).

and the IGBT GPA, respectively. The dc bus voltage for each H-bridge is 650 and 425 V for the SiC GPA and the IGBT GPA, respectively, resulting in the same overall dc bus voltage of 1300 V. The bandwidth is around 10 kHz and around 7 kHz for the SiC GPA and the IGBT GPA, respectively. Fig. 27 clearly shows that the SiC GPA is able to significantly better suppress the fixed-frequency spurious signals in the GPA output current, due to its higher bandwidth and faster switching frequency. In particular, the suppression in the peak spurious signal is improved by a factor of 3.6. Table V shows the experimental comparison of the GPA resolution indicator $\sigma(I_{\mathrm{G}})$ between the SiC GPA and the IGBT GPA. It is clear that the GPA resolution can be

TABLE V
RESOLUTION OF THE SIC GPA AND CONVENTIONAL IGBT GPA FOR DIFFERENT CURRENT LEVELS AND PULSE WIDTHS

Output Current (A)	*Pulse Width* (ms)	$\sigma(I_G)$ - *IGBT* (μAs)	$\sigma(I_G)$ - *SiC* (μAs)
100	1	2.69	2.50
	5	2.95	2.67
	10	3.09	2.78
200	1	3.37	2.84
	5	3.63	2.86
	10	3.79	3.21
400	1	3.66	2.93
	5	4.24	3.12
	10	4.33	4.06

improved at all current levels and pulsewidths by utilizing SiC switching power devices, compared to the conventional IGBT GPA. Especially, the SiC GPA can significantly improve the resolution of shorter pulses at higher currents. The improvement is around 20% and 21% for the 1 and 5 ms pulse sequence, respectively, at 400 A output current. At high power and long pulsewidth, the resolution improvement is limited by the power supply configuration and difference in dc bus voltage, leading to more voltage droop in the SiC GPA. However, at these worse operational conditions, the SiC GPA still performs better than the IGBT GPA with better operational conditions. These experimental results validate that SiC switching power devices not only have the well-known benefits of low power loss and high power densities but also can improve GPA resolution.

VI. CONCLUSION

In this article, a novel and comprehensive resolution analysis and improvement method for high-power MRI GPAs is proposed, revealing new insights in noise analysis and techniques for resolution improvement. First, a comprehensive resolution assessment of MRI GPAs is provided, as well as the impact on MRI system performance. This resolution characterization and modeling reveals the statistical relationship between MRI image quality, GPA resolution, and GPA output noise, indicating the direction for GPA resolution improvement. Second, this study establishes the GPA resolution analysis methods with respect to the most critical influencing factors. This work appears to be the first study on statistical analysis methods for evaluating GPA resolution, enabling a prediction of GPA resolution before going into the GPA design. Finally, this study introduces several novel GPA resolution improvement approaches, ensuring the realization of a high-resolution GPA.

Specifically, the proposed resolution analysis and improvement method can improve GPA resolution in the following ways.

1) bandwidth optimization can suppress most of the noise and disturbance in GPA including the most critical influencing factor of dc power supply disturbance;

2) pseudorandom code modulation reduces the fixed-frequency spurious signals in digital PWM generation;
3) utilizing SiC switching power devices in the GPA can significantly reduce spurious signals at switching frequencies and further enhance bandwidth optimization methods.

The latter reveals that SiC switching power devices not only have the well-known benefits of lower power loss and higher power densities but also can improve GPA resolution. In addition, the proposed resolution improvement methods can considerably reduce the engineering development costs and effort, since conventional low noise hardware designs require extensive prototyping, iterative tuning process and more expensive hardware platforms.

The effectiveness of the proposed design method has been experimentally validated in a 1000 V / 400 A SiC GPA demonstrator. The experimental results show a 3.6 times reduction in the peak spurious signal and a resolution improvement at all current levels and pulse lengths, compared to a conventional IGBT GPA. These experimental results validate the proposed comprehensive analysis and design methods.

This study has a number of important implications for future practice. It gives new insight in designing GPAs for optimal resolution, and provides the designer of high-accuracy amplifiers with the tools to review the design as well as tools to experimentally evaluate the implementation of the design. In this way, this article helps both understanding methods for resolution improvement, as well as pinpointing the key points designers have to address in order to ensure meeting the stringent requirements in GPA for various MRI applications. Finally, the proposed resolution analysis and improvement method can also be extended to MRI RF amplifiers and amplifiers for other high-power and high-resolution applications, such as nano-scale-positioning and subsea communication.

ACKNOWLEDGMENT

The authors would like to thank the experts in Philips Healthcare Suzhou for their advice and technical support.

REFERENCES

[1] E. Mark Haacke, R. W. Brown, M. R. Thompson, and R. Venkatesan, *Magnetic Resonance Imaging Physical Principle and Sequence Design*. New York, NY, USA: WILEY-LISS, 1999.
[2] J. A. Sabaté, R. R. Wang, F. Tao, and S. Chi, "Magnetic resonance imaging power: High-performance MVA gradient drivers," *IEEE J. Emerg. Sel. Topics Power Electron.*, vol. 4, no. 1, pp. 280–292, Sep. 2016.
[3] P. C. Loh, D. G. Holmes, and T. Lipo, "Implementation and control of distributed PWM cascaded multilevel inverters with minimal harmonic distortion and common-mode voltage," *IEEE Trans. Power Electron.*, vol. 20, no. 1, pp. 90–99, Jan. 2005.
[4] H. Takano, S. Watanabe, and M. Nakaoka, "Multiple-bridge PWM current-regulated power amplifier for magnetic resonance imaging system and its feasible digital control implementation," in *Proc. 25th Annu. Conf. IEEE Ind. Electron. Soc.*, 1999, vol. 2, pp. 785–790.
[5] L. Chen, T. Zhang, and J. Xu, "High power PWM amplifier with coupling inductor based parallel structure for magnetic resonance imaging," in *Proc. IEEE Appl. Power Electron. Conf. Expo.*, Mar. 2017, pp. 2853–2858.
[6] R. Wang, J. Sabate, E. Delgado, F. Tao, X. Liu, and B. Rowden, "High performance two H-bridge in cascaded gradient driver design with SiC power MOSFET," in *Proc. 17th Eur. Conf. Power Electron. Appl.*, 2015, pp. 1–9.
[7] K. Misha, H. Laszlo, H. He, S. Zhiyu, and J. Hongyuan, "Balancing control of paralleled full-bridge converters in high-current gradient amplifiers for MRI applications," in *Proc. Appl. Power Electron. Conf. Expo.*, 2020, pp. 1222–1229.
[8] R. Lai, L. Wang, J. Sabate, A. Elasser, and L. Stevanovic, "High-voltage high-frequency inverter using 3.3kV SiC MOSFETs," in *Proc. 15th Int. Power Electron. Motion Control Conf.*, 2012, pp. DS2b.6–1–DS2b.6–5.
[9] R. Wang, J. Sabate, X. Liu, and K. Mainali, "High efficiency power converter with SiC power MOSFETs for pulsed power applications," in *Proc. IEEE Energy Convers. Congr. Expo.*, Oct. 2017, pp. 925–930.
[10] R. Wang, J. Sabate, F. Tao, F. Xu, X. Liu, and C. Li, "H-bridge building block with SiC power MOSFETs for pulsed power applications," in *Proc. IEEE Energy Convers. Congr. Expo.*, Sep. 2016, pp. 1–6.
[11] M. Mauerer, A. Tüysüz, and J. W. Kolar, "Distortion analysis of low-THD/high-bandwidth GaN/SiC class-D amplifier power stages," in *Proc. IEEE Energy Convers. Congr. Expo.*, Sep. 2015, pp. 2563–2571.
[12] R. Lai, L. Wang, and J. Sabate, "A high efficiency two-phase interleaved inverter for wide range output waveform generation," in *Proc. IEEE Energy Convers. Congr. Expo.*, 2012, pp. 4533–4537.
[13] V. Z. Lazarevic *et al.*, "High-efficiency high-bandwidth four-quadrant fully digitally controlled GaN-based tracking power supply system for linear power amplifiers," *IEEE J. Emerg. Sel. Topics Power Electron.*, vol. 7, no. 2, pp. 664–678, Jun. 2019.
[14] Y. Lee, J. Kim, B. Han, and J. Lee, "Auxiliary resonant commutated pole inverter with clamping diodes for voltage stress reduction across auxiliary switches," in *Proc. TENCON*, 2018, pp. 0394–0398.
[15] Z. Wenzhi and Y. Xibo, "Experimental evaluation of SiC MOSFETs in comparison to Si IGBTs in a soft-switching converter," *IEEE Trans. Ind. Appl.*, vol. 56, no. 5, pp. 5108–5118, Jun. 2020.
[16] Z. Wenzhi, Y. Xibo, and L. Lan, "Performance comparison of the auxiliary resonant commutated pole inverter (ARCPI) using SiC MOSFETs or Si IGBTs," in *Proc. IEEE Energy Convers. Congr. Expo.*, Sep. 2019, pp. 1981–1987.
[17] R. Wang, J. Sabate, Y. Mei, J. Xiao, and S. Chi, "Phase-shift soft-switching power amplifier with lower EMI noise," in *Proc. IEEE Energy Convers. Congr. Expo.*, Sep. 2014, pp. 2767–2772.
[18] M. D. Bellar, T. S. Wu, A. Tchamdjou, J. Mahdavi, and M. Ehsani, "A review of soft-switched DC-AC converters," *IEEE Trans. Ind. Appl.*, vol. 34, no. 4, pp. 847–860, Jul./Aug. 1998.
[19] D. C. Hamill and P. T. Krein, "'Zero' ripple technique applicable to any DC converter," in *Proc. IEEE Annu. Power Electron. Spec. Conf.*, Jul. 1999, pp. 1165–1171, doi: 10.1109/pesc.1999.785659.
[20] M. J. Schutten, R. L. Steigerwald, and J. A. Sabaté, "Ripple current cancellation circuit," in *Proc. IEEE Appl. Power Electron. Conf. Expo.*, Feb. 2003, pp. 464–470.
[21] J. Sabate, M. Schutten, R. Steigerwald, L. Qiming, and W. F. Wirth, "Ripple cancellation filter for magnetic resonance imaging gradient amplifiers," in *Proc. IEEE Appl. Power Electron. Conf. Expo.*, Feb. 2004, pp. 792–796.
[22] M. Mauerer and J. W. Kolar, "Noise minimization for ultra-high SNR class-D power amplifiers," *CPSS Trans. Power Electron. Appl.,* vol. 3, no. 4, pp. 339–351, 2018.
[23] M. Mauerer and J. W. Kolar, "Distortion minimization for ultra-low THD class-D power amplifiers," *CPSS Trans. Power Electron. Appl.,* vol. 3, no. 4, pp. 324–338, 2018, doi: 10.24295/cpsstpea.2018.00032.
[24] R. Lai, M. Harfman Todorovic, and J. Sabate, "Analysis and suppression of a common mode resonance in the cascaded H-bridge multilevel inverter," in *Proc. IEEE Energy Convers. Congr. Expo.*, Sep. 2010, pp. 4564–4568.
[25] Z. Zhang and L. Xu, "Dead-time compensation of inverters considering snubber and parasitic capacitance," *IEEE Trans. Power Electron.*, vol. 29, no. 6, pp. 3179–3187, Aug. 2014.
[26] J. Sabate, L. J. Garce, P. M. Szczesny, and W. Skeffington, "Dead-time compensation for a high-fidelity voltage fed inverter," in *Proc. IEEE Power Electron. Spec. Conf.*, Jun. 2008, pp. 4419–4425.
[27] Y. Ji, Y. Yang, J. Zhou, H. Ding, X. Guo, and S. Padmanaban, "Control strategies of mitigating dead-time effect on power converters: An overview," *Electronics (Switzerland),* vol. 8, no. 2, Feb. 2019, Art. no. 196.
[28] L. F. S. Alves, P. Lefranc, P. O. Jeannin, and B. Sarrazin, "A new gate drive power supply configuration for common mode conducted emi reduction in phase-shifted full-bridge converter," *IEEE Trans. Power Electron.*, vol. 36, no. 4, pp. 4081–4090, Sep. 2021.
[29] M. Mauerer, A. Tuysuz, and J. W. Kolar, "Low-Jitter GaN E-HEMT gate driver with high common-mode voltage transient immunity," *IEEE Trans. Ind. Electron.,* vol. 64, no. 11, pp. 9043–9051, Mar. 2017.

[30] M. Mauerer, A. Tüysüz, and J. W. Kolar, "Low-noise isolated digital shunt for precision class-D power amplifiers," *IEEE Trans. Power Electron.*, vol. 33, no. 3, pp. 1907–1910, Aug. 2018.
[31] C. D. Motchenbacher and J. A. Connely, *Low Noise Electronic System Design*. New York, NY, USA: Wiley, 1993.
[32] G. Vailescu, *Electronic Noise and Interfering Signals – Principle and Applications*. Berlin, Germany: Springer, 2005.
[33] D. Costinett, M. Rodriguez, and D. Maksimovic, "Simple digital pulse width modulator under 100 ps resolution using general-purpose FPGAs," *IEEE Trans. Power Electron.*, vol. 28, no. 10, pp. 4466–4472, Dec. 2013.
[34] S. C. Huerta, A. de Castro, O. GarcÍa, and J. A. Cobos, "FPGA-based digital pulsewidth modulator with time resolution under 2 ns," *IEEE Trans. Power Electron.*, vol. 23, no. 6, pp. 3135–3141, Oct. 2008.
[35] X. Cheng, R. Song, G. Xie, Y. Zhang, and Z. Zhang, "A new FPGA-based segmented delay-line DPWM with compensation for critical path delays," *IEEE Trans. Power Electron.*, vol. 33, no. 12, pp. 10794–10802, Oct. 2018.
[36] W. Kester, *Data Conversion Handbook*. Amsterdam, The Netherlands: Elsevier, 2005.
[37] D. W. McRobbie *et al.*, *MRI from Picture to Proton*. 2nd ed. Cambridge, U.K.: Cambridge Univ. Press, 2006.
[38] Y. Wang, X. Xin, F. Liu, and S. Crozier, "Spiral gradient coil design for use in cylindrical MRI systems," *IEEE Trans. Biomed. Eng.*, vol. 65, no. 4, pp. 911–920, Apr. 2018.
[39] X. Du *et al.*, "Design of cylindrical transverse gradient coil for 1.5 T MRI system," *IEEE Trans. Appl. Supercond.*, vol. 22, no. 3, pp. 4402004–4402004, Jun. 2012, Art no. 4402004.
[40] R. Turner, "Gradient coil design: A review of methods," *Magn. Reson. Imag.*, vol. 11, pp. 903–920, 1993.
[41] L. Chen, T. Zhang, and J. Xu, "High power PWM amplifier with coupling inductor based parallel structure for magnetic resonance imaging," in *Proc. IEEE Appl. Power Electron. Conf. Expo.*, Mar. 2017, pp. 2853–2858.

Keqiu Zeng (Member, IEEE) was born in Fujian, China, in 1982. He received the B.S. and M.S. degrees in circuits and systems from the University of Electronic Science and Technology of China, Chengdu, China, in 2005 and 2008, respectively.

From 2008 to 2010, he was with GE Global Research Center as a Research Scientist working on medical systems. Since 2011, he has been with the Philips Healthcare Suzhou, Suzhou, China, and Philips Research Shanghai, Shanghai, China, as a Senior Research Scientist, and from 2020 as an R&D Director. He leads various research activities related to power electronics and radio frequency electronics for medical systems. His research interests include packaging and integration in power electronics, wide band gap power electronics, modern control, advanced digital signal processing, as well as radio frequency circuit and system.

Jelena Popovic (Member, IEEE) received the Dipl. Ing. degree in electrical engineering from the Faculty of Electrical Engineering, University of Belgrade, Belgrade, Serbia, in 2001, and the Ph.D. degree in electrical engineering from the Delft University of Technology, Delft, The Netherlands, in 2005.

From 2005 to 2011, she was with the European Center for Power Electronics as a Technology Transfer Coordinator. From 2008 to 2017, she was with the Delft University of Technology as an Assistant Professor. In 2018, she co-founded a start-up in energy access, Klimop Energy. Since October 2019, she joined the University of Twente, Enschede, The Netherlands, as a part-time Associate Professor to develop an energy access programme.

She has published more than 100 publications in scientific journals, magazines, and conferences. Her recent interests include bottom-up solutions for energy access, appropriate technology and socio-technical integration.

Dr. Popovic is a Vice-Chair of the IEEE PELS Technical Committee TC-12 Energy Access and Off-Grid Systems and the IEEE Empower a Billion Lives Competition.

Gert Rietveld (Senior Member, IEEE) received the M.Sc. (cum laude) and Ph.D. degrees in applied physics from Delft University of Technology, Delft, The Netherlands, in 1988 and 1993, respectively.

Since 1993, he has been with VSL, Delft, the national measurement institute of The Netherlands, where he currently is a Chief Scientist in the electricity and time department. He has more than 25 years of experience in the area of electrical metrology, with his present work focusing on precision measurements for power and energy, and particularly metrology for smart electricity grids. He also is a Full Professor with the University of Twente, Enschede, The Netherlands, where he holds a chair on "Power and Energy Measurement Systems," working on precision measurements on batteries, measurement of power converter efficiency, and monitoring of electricity grids.

Dr. Rietveld chairs the European Metrology Network on Smart Electricity Grids. He is a member of the International Committee for Weights and Measures (CIPM) in Paris and President of its Consultative Committee for Electricity and Magnetism (CCEM). He is an active member of several IEEE, CIGRÉ, CENELEC, and IEC working groups.

Saijun Mao (Senior Member, IEEE) received the B.S. and M.S. degrees from the Nanjing University of Aeronautics and Astronautics, Nanjing, China, and the Ph.D. degree from Delft University of Technology, Delft, The Netherlands, all in electrical engineering, in 2003, 2006, and 2018, respectively.

From 2006 to 2017, he was a Senior Engineer and Project Leader with the GE Global Research Center. He is currently a Research Fellow with Fudan University, Shanghai, China. He has published more than 50 IEEE conference and journal papers. He holds more than 50 issued patents and pending patent applications. His research interests include wide-bandgap power semiconductor devices-based power conversion systems, high-frequency high-voltage generator systems, as well as harsh environment power conversion and packaging.

Dr. Mao was the tutorial instructor in eight premier IEEE power electronics conferences. He was the recipient of one IEEE Best Paper award, also more than 15 awards, including the Annual Technology Excellence Award, the Annual Technology Excellence Team Award, and the Top Inventor Award in GE Global Research Center.

Hui Yu (Member, IEEE) was born in Jiangsu, China, in 1988. He received the B.S. degree in electrical engineering from Nanjing University of Aeronautics and Astronautics, Nanjing, China, in 2008.

From 2011 to 2014, he was with Efore Suzhou as a Power Electronics Engineer. Since 2015, he has been with the Philips Healthcare Suzhou, Suzhou, China, as a Senior Power Electronics Engineer. His research interests include design and control of power electronics systems, high power density power system, and electrical magnetic interference.

Liguo Wang (Member, IEEE) was born in Zhejiang, China, in 1989. He received the B.S. degree in natural science physics from Lishui University, Lishui, China, in 2011, and the M.Sc. degree in natural science physics from Zhejiang University, Hangzhou, China, in 2013.

From 2013 to 2015, he was with the Shanghai Institute of Optics and Fine Mechanics. Since 2017, he has been with Philips Healthcare Suzhou, Suzhou, China, as a Senior Digital Signal Processing Engineer. His research interests include advanced digital signal processing and modern control.

Kun Liu (Member, IEEE) was born in Chongqing, China, in 1976. He received the B.S. and M.S. degrees in signal and information processing from Chongqing University, Chongqing, China, in 2003.

From 2004 to 2011, he was with the 10th Institute of China Electronics Technology and Huawei Hisilicon as a Digital Design Engineer. Since 2012, he has been with Philips Healthcare Suzhou, Suzhou, China, as a Senior Digital Processing Engineer. His research interests include digital signal processing and soft define radio.

Zhiding Zhou (Member, IEEE) was born in Anhui, China, in 1992. He received the B.S. degree in digital systems engineering from the University of Central Lancashire, Preston, U.K., in 2014, and the M.S. degree in digital systems engineering from the University of York, York, U.K., in 2016.

From 2017 to 2020, he was with Nanjing Gova as a Design Engineer. Since 2020, he has been with Philips Healthcare Suzhou, Suzhou, China, as a Digital Processing Engineer. His research interests include modern control and digital signal processing.